

Mass balance of the Antarctic Ice Sheet from 1992 to 2017

The IMBIE team*

The Antarctic Ice Sheet is an important indicator of climate change and driver of sea-level rise. Here we combine satellite observations of its changing volume, flow and gravitational attraction with modelling of its surface mass balance to show that it lost $2,720 \pm 1,390$ billion tonnes of ice between 1992 and 2017, which corresponds to an increase in mean sea level of 7.6 ± 3.9 millimetres (errors are one standard deviation). Over this period, ocean-driven melting has caused rates of ice loss from West Antarctica to increase from 53 ± 29 billion to 159 ± 26 billion tonnes per year; ice-shelf collapse has increased the rate of ice loss from the Antarctic Peninsula from 7 ± 13 billion to 33 ± 16 billion tonnes per year. We find large variations in and among model estimates of surface mass balance and glacial isostatic adjustment for East Antarctica, with its average rate of mass gain over the period 1992–2017 (5 ± 46 billion tonnes per year) being the least certain.

The ice sheets of Antarctica hold enough water to raise global sea level by 58 m^1 . They channel ice to the oceans through a network of glaciers and ice streams², each with a substantial inland catchment³. Fluctuations in the mass of grounded ice sheets arise owing to differences between net snow accumulation at the surface, meltwater runoff and ice discharge into the ocean. In recent decades, reductions in the thickness⁴ and extent⁵ of floating ice shelves have disturbed inland ice flow, triggering retreat^{6,7}, acceleration^{8,9} and drawdown^{10,11} of many marine-terminating ice streams. Various techniques have been developed to measure changes in ice-sheet mass, based on satellite observations of their speed¹², volume¹³ and gravitational attraction¹⁴ combined with modelled surface mass balance (SMB)¹⁵ and glacial isostatic adjustment (GIA; the ongoing movement of land associated with changes in ice loading)¹⁶. Since 1989, there have been more than 150 assessments of ice loss from Antarctica based on these approaches¹⁷. An inter-comparison of 12 such estimates¹⁸ demonstrated that the three principal satellite techniques provide similar results at the continental scale and, when combined, lead to an estimated mass loss of 71 ± 53 billion tonnes of ice per year (Gt yr^{-1}) averaged over the period 1992–2011 (errors are one standard deviation unless stated otherwise). Here, we extend this assessment to include twice as many studies, doubling the overlap period and extending the record to 2017.

Satellite observations

We collated 24 independently derived estimates of ice-sheet mass balance (Fig. 1) that were determined within the period 1992–2017 and based on the techniques of satellite altimetry (seven estimates), gravimetry (15 estimates) or the input–output method (two estimates). Altogether, 24, 24 and 23 individual estimates of mass change were computed within defined geographical limits^{3,19} for the East Antarctic Ice Sheet (EAIS), West Antarctic Ice Sheet (WAIS) and Antarctic Peninsula Ice Sheet (APIS), respectively. We compared the rates of ice-sheet mass change (see Methods) over common intervals of time¹⁸. We then averaged the rates of ice-sheet mass balance using the same class of satellite observations to produce three technique-dependent time series of mass change in each geographical region (see Methods). Within each class, we computed the uncertainty in the annual mass rate as the mean uncertainty of the individual

contributions. The final, reconciled estimate of ice-sheet mass change for each region was computed as the mean of the technique-dependent values available at each epoch (Fig. 1). In computing the associated uncertainty, we assume that the errors for each technique are independent. To estimate the cumulative mass change and its uncertainty (Fig. 2), we integrated the reconciled estimates for each ice sheet and weighted the annual uncertainty by $1/\sqrt{n}$, where n is the number of years since the start of each time series. We computed Antarctic Ice Sheet (AIS) mass trends as the linear sum of the regional trends and the uncertainties in the mass trends as the root-sum-square of the regional uncertainties (Table 1).

Trends in Antarctic ice-sheet mass

The level of disagreement between individual estimates of ice-sheet mass balance increases with the area of each ice-sheet region, with average per-epoch standard deviations of 11 Gt yr^{-1} , 21 Gt yr^{-1} and 37 Gt yr^{-1} at the APIS, the WAIS and the EAIS, respectively (Fig. 1, Methods). Among the techniques, gravimetric estimates are the most abundant and also the most closely aligned, although their spread increases in East Antarctica, where GIA remains poorly constrained²⁰ and is least certain when spatially integrated^{21–32}, owing to the vast extent of the region. Solutions based on satellite altimetry and the input–output method run for the entire record, roughly twice the duration of the gravimetry time series. Although most (59%) estimates are within one standard deviation of the technique-dependent mean, a few (6%) depart by more than three standard deviations. At the Antarctic Peninsula, the 25-year average rate of ice-sheet mass balance is $-20 \pm 15 \text{ Gt yr}^{-1}$, with an increase of about 15 Gt yr^{-1} in losses since 2000. The strongest signal and trend has occurred in West Antarctica, where rates of mass loss increased from $53 \pm 29 \text{ Gt yr}^{-1}$ to $159 \pm 26 \text{ Gt yr}^{-1}$ between the first and final five years of our survey; the largest increase occurred during the late 2000s when ice discharge from the Amundsen Sea sector accelerated³³. Both of these regional losses are driven by reductions in the thickness and extent of floating ice shelves, which has triggered the retreat, acceleration and drawdown of marine-terminating glaciers³⁴. The least certain result is in East Antarctica, where the average 25-year mass trend is $5 \pm 46 \text{ Gt yr}^{-1}$. Overall, the AIS lost $2,720 \pm 1,390 \text{ Gt}$ of ice between 1992 and 2017, an average rate of $109 \pm 56 \text{ Gt yr}^{-1}$.

*A list of authors and their affiliations appears at the end of the paper.

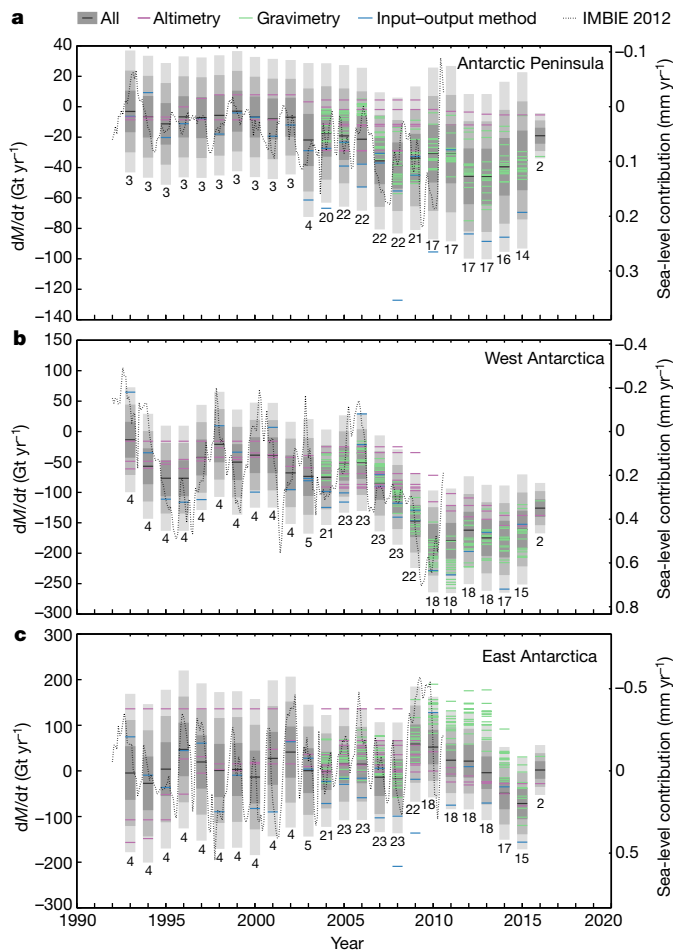


Fig. 1 | Antarctic Ice Sheet mass balance. **a–c**, Rate of mass change (dM/dt) of the APIS (**a**), WAIS (**b**) and EAIS (**c**), as determined from the various satellite-altimetry (purple), input-output-method (blue) and gravimetry (green) assessments included in this study. In each case, dM/dt is computed from time series of relative mass change using a three-year window at annual intervals. An average of estimates across each class of measurement technique is also shown for each year (black). The estimated 1σ , 2σ and 3σ ranges of the class averages are shaded in dark, mid and light grey, respectively; the number of individual mass-balance estimates collated at each epoch is shown below.

Surface mass balance

Knowledge of the ice-sheet SMB is an essential component of the input–output method, which subtracts solid-ice discharge from net snow accumulation, and aids interpretation of mass trends derived from satellite altimetry and gravimetry. Snowfall is the main driver of temporal and spatial variability in AIS surface mass change^{35,36}. Although locally important, spatially integrated sublimation and melt-water runoff are typically one and two orders of magnitude smaller, respectively. In the absence of observation-based maps, AIS SMB is usually taken from atmospheric models, evaluated with in situ and remotely sensed observations^{15,37–40}. To assess Antarctic SMB, we compared two global reanalysis products (JRA55 and ERA-Interim) and two regional climate models (RACMO2 and MARv3.6) (see Methods). ERA-Interim is usually regarded as the best-performing reanalysis product over Antarctica, albeit with a dry bias in the interior and overestimated rain fraction^{39,41,42}. Spatially averaged accumulation rates peak at the Antarctic Peninsula, and are roughly three and seven times lower in West and East Antarctica, respectively (Extended Data Figs. 2, 3). Compared to the all-model average SMB of $1,994 \text{ Gt yr}^{-1}$, the regional climate models give values 4.7% higher and the reanalyses 7% lower. These differences can be attributed to the higher resolution of the regional models, which resolve the steep coastal precipitation

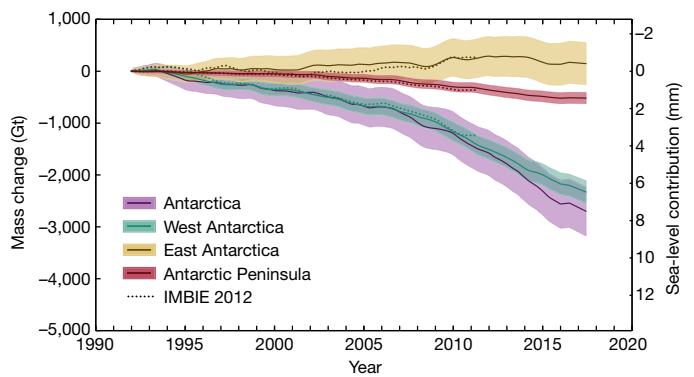


Fig. 2 | Cumulative Antarctic Ice Sheet mass change. The cumulative ice-sheet mass changes (solid lines) are determined from the integral of monthly measurement-class averages (for example, the black lines in Fig. 1) for each ice sheet. The estimated 1σ uncertainty of the cumulative change is shaded. The dashed lines show the results of a previous assessment¹⁸.

gradients in greater detail, and to their improved representation of polar processes. The temporal variability of all products is similar and they all agree on the absence of an ice-sheet-wide trend in SMB over the period 1979–2017, which implies that recent mass loss from the AIS is dominated by increased solid-ice discharge into the ocean.

Glacial isostatic adjustment

Gravimetric estimates of mass change are strongly influenced by the method used to correct for GIA¹⁶. In this study, six different GIA models were used^{21,24,26,30,31,43}. We also assessed nine continent-wide forward-model simulations and two regional model simulations to better understand uncertainties in the GIA signal; we reprocessed the gravimetry estimates of mass balance using the W12a²⁶ and IJ05_R2³¹ GIA models for comparison with earlier work¹⁸ (see Methods). The net gravitational effect of GIA across Antarctica is positive, and the mean and standard deviation of the continent-wide GIA models ($54 \pm 18 \text{ Gt yr}^{-1}$) is very close to that of the W12a ($56 \pm 27 \text{ Gt yr}^{-1}$) and IJ05_R2 ($55 \pm 13 \text{ Gt yr}^{-1}$) models. The narrow spread probably reflects the difficulty of quantifying the timing and extent of past ice-sheet change and the absence of lateral variations in Earth rheology within some models⁴⁴. Models predict the greatest rates of solid-Earth uplift ($5\text{--}7 \text{ mm yr}^{-1}$ on average) in areas where GIA is a substantial component of the regional mass change, such as the Amundsen, Ross and Filchner–Ronne sectors of West Antarctica (see Extended Data Fig. 4), but also the greatest variability (for example, a standard deviation of more than 10 mm yr^{-1} in the Amundsen sector). Away from areas with large GIA signals there is low variance among the models and broad agreement with GPS observations⁴⁵. Nevertheless, most models considered here do not account for ice-sheet change during the past few millennia, because it is poorly known. Inaccurate treatment of low-degree harmonics associated with the global GIA signal can also bias gravimetric mass-balance calculations⁴⁶. If the GIA signal includes a transient component associated with recent ice-sheet change, it will bias mass-trend estimates and should be accounted for in future work.

Outlook

Improvements in assessments of ice-sheet mass balance are still possible. Airborne snow radar^{47,48} is a powerful tool for evaluating models of SMB and firn compaction over large spatial (thousands of kilometres) and temporal (centennial) scales, in addition to the ice cores that have traditionally been used⁴⁹. Geological constraints on the ice-sheet history²⁰ and GPS measurements of contemporary uplift^{45,50} enable GIA models to be scrutinized and calibrated. More of both of these types of datasets are needed, especially in East Antarctica. Given their apparent diversity, the spread of models of GIA and SMB should be evaluated in concert with the satellite gravimetry, altimetry and velocity measurements. A reassessment of the satellite measurements acquired during

Table 1 | Rates of ice-sheet mass change

	1992–1997 (Gt yr ⁻¹)	1997–2002 (Gt yr ⁻¹)	2002–2007 (Gt yr ⁻¹)	2007–2012 (Gt yr ⁻¹)	2012–2017 (Gt yr ⁻¹)	1992–2011 (Gt yr ⁻¹)	1992–2017 (Gt yr ⁻¹)
EAIS	11 ± 58	8 ± 56	12 ± 43	23 ± 38	-28 ± 30	13 ± 50	5 ± 46
WAIS	-53 ± 29	-41 ± 28	-65 ± 27	-148 ± 27	-159 ± 26	-73 ± 28	-94 ± 27
APIS	-7 ± 13	-6 ± 13	-20 ± 15	-35 ± 17	-33 ± 16	-16 ± 14	-20 ± 15
AIS	-49 ± 67	-38 ± 64	-73 ± 53	-160 ± 50	-219 ± 43	-76 ± 59	-109 ± 56

Rates were determined from all satellite measurements over various epochs for the EAIS, WAIS and APIS, which combined constitute the AIS. The period 1992–2011 is included for comparison to a previous assessment¹⁸, which reported mass-balance estimates of 14 ± 43 Gt yr⁻¹ for the EAIS, -65 ± 26 Gt yr⁻¹ for the WAIS, -20 ± 14 Gt yr⁻¹ for the APIS and -71 ± 53 Gt yr⁻¹ for the AIS. The small differences in our updated estimates for this period are due to our inclusion of more data. Errors are 1 σ .

the 1990s would address the imbalance that is present in the current record. Alternative techniques (see, for example, ref. ⁵¹) for combining satellite datasets should be explored, and satellite measurements with common temporal sampling should be contrasted. The ice-sheet mass-balance record should now be separated into the contributions due to short-term fluctuations in SMB and to longer-term trends in glacier ice. In addition to these improvements, continued satellite observations are, of course, essential.

Online content

Any Methods, including any statements of data availability and Nature Research reporting summaries, along with any additional references and Source Data files, are available in the online version of the paper at <https://doi.org/10.1038/s41586-018-0179-y>

Received: 12 April 2018; Accepted: 24 April 2018;

- Fretwell, P. et al. Bedmap2: improved ice bed, surface and thickness datasets for Antarctica. *Cryosphere* **7**, 375–393 (2013).
- Rignot, E., Mouginot, J. & Scheuchl, B. Ice flow of the Antarctic ice sheet. *Science* **333**, 1427–1430 (2011).
- Zwally, H. J., Giovinetto, M. B., Beckley, M. A. & Saba, J. L. Antarctic and Greenland drainage systems. *GSFC Cryospheric Sciences Laboratory* http://icesat4.gsfc.nasa.gov/cryo_data/ant_grn_drainage_systems.php (2012).
- Shepherd, A. et al. Recent loss of floating ice and the consequent sea level contribution. *Geophys. Res. Lett.* **37**, L13503 (2010).
- Cook, A. J. & Vaughan, D. G. Overview of areal changes of the ice shelves on the Antarctic Peninsula over the past 50 years. *Cryosphere* **4**, 77–98 (2010).
- Rignot, E., Mouginot, J., Morlighem, M., Seroussi, H. & Scheuchl, B. Widespread, rapid grounding line retreat of Pine Island, Thwaites, Smith, and Kohler glaciers, West Antarctica, from 1992 to 2011. *Geophys. Res. Lett.* **41**, 3502–3509 (2014).
- Konrad, H. et al. Net retreat of Antarctic glacier grounding lines. *Nat. Geosci.* **11**, 258–262 (2018).
- Joughin, I., Tulaczyk, S., Bindschadler, R. & Price, S. F. Changes in west Antarctic ice stream velocities: observation and analysis. *J. Geophys. Res. Solid Earth* **107**, 2289 (2002).
- Rignot, E. et al. Accelerated ice discharge from the Antarctic Peninsula following the collapse of Larsen B ice shelf. *Geophys. Res. Lett.* **31**, L18401 (2004).
- Shepherd, A., Wingham, D. J. & Mansley, J. A. D. Inland thinning of the Amundsen Sea sector, West Antarctica. *Geophys. Res. Lett.* **29**, <https://doi.org/10.1029/2001GL014183> (2002).
- Scambos, T. A., Bohlander, J. A., Shuman, C. A. & Skvarca, P. Glacier acceleration and thinning after ice shelf collapse in the Larsen B embayment, Antarctica. *Geophys. Res. Lett.* **31**, L18402 (2004).
- Rignot, E. & Thomas, R. H. Mass balance of polar ice sheets. *Science* **297**, 1502–1506 (2002).
- Wingham, D. J., Ridout, A. J., Scharroo, R., Arthern, R. J. & Shum, C. K. Antarctic elevation change from 1992 to 1996. *Science* **282**, 456–458 (1998).
- Velicogna, I. & Wahr, J. Measurements of time-variable gravity show mass loss in Antarctica. *Science* **311**, 1754–1756 (2006).
- van Wessem, J. M. et al. Modelling the climate and surface mass balance of polar ice sheets using RACMO2 – part 2: Antarctica (1979–2016). *Cryosphere* **12**, 1479–1498 (2018).
- King, M. A. et al. Lower satellite-gravimetry estimates of Antarctic sea-level contribution. *Nature* **491**, 586–589 (2012).
- Briggs, K. et al. Charting ice-sheet contributions to global sea-level rise. *Eos* **97**, <https://doi.org/10.1029/2016EO055719> (2016).
- Shepherd, A. et al. A reconciled estimate of ice-sheet mass balance. *Science* **338**, 1183–1189 (2012).
- Rignot, E., Mouginot, J. & Scheuchl, B. Antarctic grounding line mapping from differential satellite radar interferometry. *Geophys. Res. Lett.* **38**, L10504 (2011).
- Bentley, M. J. et al. A community-based geological reconstruction of Antarctic Ice Sheet deglaciation since the Last Glacial Maximum. *Quat. Sci. Rev.* **100**, 1–9 (2014).
- Peltier, W. R. Global glacial isostasy and the surface of the ice-age Earth: the ICE-5G (VM2) model and GRACE. *Annu. Rev. Earth Planet. Sci.* **32**, 111–149 (2004).
- A. G., Wahr, J. & Zhong, S. Computations of the viscoelastic response of a 3-D compressible earth to surface loading: an application to glacial isostatic adjustment in Antarctica and Canada. *Geophys. J. Int.* **192**, 557–572 (2013).
- Sasgen, I. et al. Antarctic ice-mass balance 2003 to 2012: regional reanalysis of GRACE satellite gravimetry measurements with improved estimate of glacial-isostatic adjustment based on GPS uplift rates. *Cryosphere* **7**, 1499–1512 (2013).
- Peltier, W. R., Argus, D. F. & Drummond, R. Space geodesy constrains ice age terminal deglaciation: the global ICE-6G-C (VM5a) model. *J. Geophys. Res. Solid Earth* **120**, 450–487 (2015).
- King, M. A., Whitehouse, P. L. & van der Wal, W. Incomplete separability of Antarctic plate rotation from glacial isostatic adjustment deformation within geodetic observations. *Geophys. J. Int.* **204**, 324–330 (2016).
- Whitehouse, P. L., Bentley, M. J., Milne, G. A., King, M. A. & Thomas, I. D. A new glacial isostatic adjustment model for Antarctica: calibrated and tested using observations of relative sea-level change and present-day uplift rates. *Geophys. J. Int.* **190**, 1464–1482 (2012).
- Spada, G., Melini, D. & Colleoni, F. SELEN v2.9.12, <https://geodynamics.org/cig/software/selen/> (Computational Infrastructure for Geodynamics, 2015).
- Konrad, H., Sasgen, I., Pollard, D. & Klemann, V. Potential of the solid-Earth response for limiting long-term West Antarctic Ice Sheet retreat in a warming climate. *Earth Planet. Sci. Lett.* **432**, 254–264 (2015).
- Briggs, R. D., Pollard, D. & Tarasov, L. A data-constrained large ensemble analysis of Antarctic evolution since the Eemian. *Quat. Sci. Rev.* **103**, 91–115 (2014).
- Ivins, E. R. & James, T. S. Antarctic glacial isostatic adjustment: a new assessment. *Antarct. Sci.* **17**, 541–553 (2005).
- Ivins, E. R. et al. Antarctic contribution to sea level rise observed by GRACE with improved GIA correction. *J. Geophys. Res. Solid Earth* **118**, 3126–3141 (2013).
- Nield, G. A. et al. Rapid bedrock uplift in the Antarctic Peninsula explained by viscoelastic response to recent ice unloading. *Earth Planet. Sci. Lett.* **397**, 32–41 (2014).
- Mouginot, J., Rignot, E. & Scheuchl, B. Sustained increase in ice discharge from the Amundsen Sea Embayment, West Antarctica, from 1973 to 2013. *Geophys. Res. Lett.* **41**, 1576–1584 (2014).
- Shepherd, A., Fricker, H. A. & Farrell, S. L. Trends and connections across the Antarctic cryosphere. *Nature* **558**, <https://doi.org/10.1038/s41586-018-0171-6> (2018).
- Boening, C., Lebsack, M., Landerer, F. & Stephens, G. Snowfall-driven mass change on the East Antarctic ice sheet. *Geophys. Res. Lett.* **39**, L21501 (2012).
- Medley, B. et al. Temperature and snowfall in Western Queen Maud Land increasing faster than climate model projections. *Geophys. Res. Lett.* **45**, 1472–1480 (2018).
- Favier, V. et al. An updated and quality controlled surface mass balance dataset for Antarctica. *Cryosphere* **7**, 583–597 (2013).
- van de Berg, W. J. & Medley, B. Brief Communication: Upper-air relaxation in RACMO2 significantly improves modelled interannual surface mass balance variability in Antarctica. *Cryosphere* **10**, 459–463 (2016).
- Palermo, C. et al. Evaluation of Antarctic snowfall in global meteorological reanalyses. *Atmos. Res.* **190**, 104–112 (2017).
- Van Wessem, J. M. et al. Improved representation of East Antarctic surface mass balance in a regional atmospheric climate model. *J. Glaciol.* **60**, 761–770 (2014).
- Bromwich, D. H., Nicolas, J. P. & Monaghan, A. J. An assessment of precipitation changes over Antarctica and the southern ocean since 1989 in contemporary global reanalyses. *J. Clim.* **24**, 4189–4209 (2011).
- Behrangi, A. et al. Status of high-latitude precipitation estimates from observations and reanalyses. *J. Geophys. Res.* **121**, 4468–4486 (2016).
- Klemann, V. & Martinec, Z. Contribution of glacial-isostatic adjustment to the geocentre motion. *Tectonophysics* **511**, 99–108 (2011).
- van der Wal, W., Whitehouse, P. L. & Schrama, E. J. O. Effect of GIA models with 3D composite mantle viscosity on GRACE mass balance estimates for Antarctica. *Earth Planet. Sci. Lett.* **414**, 134–143 (2015).
- Martín-Español, A. et al. An assessment of forward and inverse GIA solutions for Antarctica. *J. Geophys. Res. Solid Earth* **121**, 6947–6965 (2016).
- Caron, L. et al. GIA model statistics for GRACE hydrology, cryosphere, and ocean science. *Geophys. Res. Lett.* **45**, 2203–2212 (2018).
- Medley, B. et al. Constraining the recent mass balance of Pine Island and Thwaites glaciers, West Antarctica, with airborne observations of snow accumulation. *Cryosphere* **8**, 1375–1392 (2014).

48. Lewis, G. et al. Regional Greenland accumulation variability from Operation IceBridge airborne accumulation radar. *Cryosphere* **11**, 773–788 (2017).
49. Thomas, E. R. et al. Regional Antarctic snow accumulation over the past 1000 years. *Clim. Past* **13**, 1491–1513 (2017).
50. Thomas, I. D. et al. Widespread low rates of Antarctic glacial isostatic adjustment revealed by GPS observations. *Geophys. Res. Lett.* **38**, L22302 (2011).
51. Wahr, J., Wingham, D. & Bentley, C. A method of combining ICESat and GRACE satellite data to constrain Antarctic mass balance. *J. Geophys. Res. Solid Earth* **105**, 16279–16294 (2000).

Acknowledgements This work is an outcome of the ESA–NASA Ice Sheet Mass Balance Inter-comparison Exercise. A.S. was additionally supported by a Royal Society Wolfson Research Merit Award and by the ESA Climate Change Initiative.

Reviewer information *Nature* thanks R. Bell and C. Hulbe for their contribution to the peer review of this work.

Author contributions A.S. and E.I. designed and led the study. E.R., B.S., M.v.d.B., I.V. and P.W. led the input–output-method, altimetry, SMB, gravimetry and GIA experiments, respectively. G.M. and M.E.P. performed the data collation and analysis. A.S., E.I., K.B., G.K., M.H., I.J., H.K., M.M., J.M., S.N., I.O., M.E.P., T.P., E.R., I.S., T.Sc., N.S., T.SI., B.S., I.V., M.v.W. and P.W. wrote and edited the manuscript. All authors participated in the data interpretation and commented on the manuscript.

Competing interests The authors declare no competing interests.

Additional information

Extended data is available for this paper at <https://doi.org/10.1038/s41586-018-0179-y>.

Supplementary information is available for this paper at <https://doi.org/10.1038/s41586-018-0179-y>.

Reprints and permissions information is available at <http://www.nature.com/reprints>.

Publisher's note: Springer Nature remains neutral with regard to jurisdictional claims in published maps and institutional affiliations.

The IMBIE team

Andrew Shepherd^{1*}, Erik Ivins², Eric Rignot³, Ben Smith⁴, Michiel van den Broeke⁵, Isabella Velicogna³, Pippa Whitehouse⁶, Kate Briggs¹, Ian Joughin⁴, Gerhard Krinner⁷, Sophie Nowicki⁸, Tony Payne⁹, Ted Scambos¹⁰, Nicole Schlegel², Geruo A³, Cécile Agosta¹¹, Andreas Ahlström¹², Greg Babonis¹³, Valentina Barletta¹⁴, Alejandro Blazquez¹⁵, Jennifer Bonin¹⁶, Beata Csatho¹³, Richard Cullather¹⁷, Denis Felikson¹⁸, Xavier Fettweis¹¹, Rene Forsberg¹⁴, Hubert Gallee⁷, Alex Gardner², Lin Gilbert¹⁹, Andreas Groh²⁰, Brian Gunter²¹, Edward Hanna²², Christopher Harig²³, Veit Helm²⁴, Alexander Horvath²⁵, Martin Horwath²⁰, Shfaqat Khan¹⁴, Kristian K. Kjeldsen^{12,26}, Hannes Konrad¹, Peter Langen²⁷, Benoit Lecavalier²⁸, Bryant Loomis⁸, Scott Luthcke⁸, Malcolm McMillan¹, Daniele Melini²⁹, Sebastian Mernild^{30,31,32}, Yara Mohajerani³,

Philip Moore³³, Jeremie Mougnot^{3,7}, Gorka Moyano³⁴, Alan Muir¹⁹, Thomas Nagler³⁵, Grace Nield⁶, Johan Nilsson², Brice Noel⁵, Ines Otosaka¹, Mark E. Pattle³⁴, W. Richard Peltier³⁶, Nadege Pie¹⁸, Roelof Rietbroek³⁷, Helmut Rott³⁵, Louise Sandberg-Sørensen¹⁴, Ingo Sasgen²⁴, Himanshu Save¹⁸, Bernd Scheuchl³, Ernst Schrama³⁸, Ludwig Schröder²⁰, Ki-Weon Seo³⁹, Sebastian Simonsen¹⁴, Tom Slater¹, Giorgio Spada⁴⁰, Tyler Sutterley³, Matthieu Talpe⁴¹, Lev Tarasov²⁸, Willem Jan van de Berg⁵, Wouter van der Wal³⁸, Melchior van Wessem⁵, Bramha Dutt Vishwakarma⁴², David Wiese² & Bert Wouters⁵

¹Centre for Polar Observation and Modelling, University of Leeds, Leeds, UK. ²NASA Jet Propulsion Laboratory, Pasadena, CA, USA. ³Department of Earth System Science, University of California, Irvine, CA, USA. ⁴Department of Earth and Space Sciences, University of Washington, Seattle, WA, USA. ⁵Institute for Marine and Atmospheric Research, Utrecht University, Utrecht, The Netherlands. ⁶Department of Geography, Durham University, Durham, UK. ⁷Institute of Environmental Geosciences, Université Grenoble Alpes, Grenoble, France. ⁸Cryospheric Sciences Laboratory, NASA Goddard Space Flight Centre, Greenbelt, MD, USA. ⁹School of Geographical Sciences, University of Bristol, Bristol, UK. ¹⁰National Snow and Ice Data Centre, University of Colorado, Boulder, CO, USA. ¹¹Department of Geography, University of Liège, Liège, Belgium. ¹²Geological Survey of Denmark and Greenland, Copenhagen, Denmark. ¹³Department of Geology, State University of New York at Buffalo, Buffalo, NY, USA. ¹⁴DTU Space, National Space Institute, Technical University of Denmark, Kongens Lyngby, Denmark. ¹⁵Spatial Geophysics and Oceanography Studies Laboratory, Toulouse, France. ¹⁶College of Marine Sciences, University of South Florida, Tampa, FL, USA. ¹⁷Earth System Science Interdisciplinary Centre, NASA Goddard Space Flight Centre, Greenbelt, MD, USA. ¹⁸Centre for Space Research, University of Texas, Austin, TX, USA. ¹⁹Mullard Space Science Laboratory, University College London, Holmbury St Mary, UK. ²⁰Institute for Planetary Geodesy, Technische Universität Dresden, Dresden, Germany. ²¹Daniel Guggenheim School of Aerospace Engineering, Georgia Institute of Technology, Atlanta, GA, USA. ²²School of Geography, University of Lincoln, Lincoln, UK. ²³Department of Geosciences, University of Arizona, Tucson, AZ, USA. ²⁴Alfred Wegener Institute, Helmholtz Centre for Polar and Marine Research, Bremerhaven, Germany. ²⁵Institute of Astronomical and Physical Geodesy, Technical University Munich, Munich, Germany. ²⁶Centre for GeoGenetics, Natural History Museum of Denmark, Copenhagen, Denmark. ²⁷Danish Meteorological Institute, Copenhagen, Denmark. ²⁸Department of Physics and Physical Oceanography, Memorial University of Newfoundland, St. John's, Newfoundland and Labrador, Canada. ²⁹Section of Seismology and Tectonophysics, National Institute of Geophysics and Volcanology, Rome, Italy. ³⁰Nansen Environmental and Remote Sensing Centre, Bergen, Norway. ³¹Faculty of Engineering and Science, Western Norway University of Applied Sciences, Sogndal, Norway. ³²Direction of Antarctic and Sub-Antarctic Programs, Universidad de Magallanes, Punta Arenas, Chile. ³³School of Civil Engineering and Geosciences, Newcastle University, Newcastle upon Tyne, UK. ³⁴isardSAT, Barcelona, Spain. ³⁵ENVEO, Innsbruck, Austria. ³⁶Department of Physics, University of Toronto, Toronto, Ontario, Canada. ³⁷Institute of Geodesy and Geoinformation, University of Bonn, Bonn, Germany. ³⁸Department of Space Engineering, Delft University of Technology, Delft, The Netherlands. ³⁹Department of Earth Science Education, Seoul National University, Seoul, South Korea. ⁴⁰Institute of Physics, University of Urbino “Carlo Bo”, Urbino, Italy. ⁴¹Aerospace Engineering Sciences, Centre for Astrodynamics Research, University of Colorado, Boulder, CO, USA. ⁴²Geodetic Institute, University of Stuttgart, Stuttgart, Germany. *e-mail: a.shepherd@leeds.ac.uk

METHODS

Data. No statistical methods were used to predetermine sample size.

We analyse five groups of data: mass-balance estimates determined from satellite altimetry, gravimetry and the input–output method, and model estimates of SMB and GIA. We compute the datasets using common spatial and temporal domains to facilitate their aggregation, according to previously reported methods (see Supplementary Table 1). In total, 24 mass-balance datasets were included. The data include 25 years of satellite-radar-altimeter measurements, 24 years of satellite input–output-method measurements and 14 years of satellite-gravimetry measurements (Extended Data Fig. 1). Among these data are estimates of ice-sheet mass balance for each ice sheet derived from each satellite technique. In comparison to the first IMBIE assessment¹⁸, new satellite missions, updated methodologies and improvements in geophysical corrections have contributed to an increase in the quantity, duration and overlap period of data used here. In addition, two new experiment groups have assessed 11 GIA and 4 SMB models. The complete list of datasets is provided in Supplementary Table 1.

Drainage basins. In this assessment, we analyse mass trends using two sets of ice-sheet drainage basins (Extended Data Fig. 2) to ensure consistency with those used in the first IMBIE assessment¹⁸ and to evaluate an updated definition tailored towards assessments using the input–output method. The first drainage-basin set was delineated using surface elevation maps derived from ICESat-1 on the basis of the provenance of the ice and includes 27 basins⁵. The second set was updated to consider other factors such as the direction of ice flow and includes 18 basins in Antarctica^{2,19}. To assess the effect of the different sets on the estimates of ice-sheet mass balance, we compared mass-balance determinations between the two delineations of ice-sheet drainage basins. This evaluation was facilitated by seven estimates (altimetry or gravimetry) determined using both sets. At the scale of the major ice-sheet divisions, the delineations produce similar total extents. By far the largest differences occur in the delineation (or definition) of East and West Antarctica, owing to differences in the position of the ice divide that separate them. Within these regions, the root-mean-square difference between 26 pairs of estimates of ice-sheet mass balance computed using the two drainage-basin sets is 8.7 Gt yr⁻¹. This difference is small in comparison to the certainty of individual assessments of ice-sheet mass balance.

Computing rates of mass change. The raw satellite mass-balance data are time series of either relative mass change $\Delta M(t)$ or the rate of mass change $dM(t)/dt$, plus their associated uncertainty, integrated over at least one of the ice-sheet regions defined in the standard drainage-basin sets. In the case of $\Delta M(t)$, the time series represents the change in mass through time relative to some nominal reference value. The duration and sampling frequency of the time series was not restricted. In practice, few mass time series were of $\Delta M(t)$ and $dM(t)/dt$. Because the inter-comparison exercise is based on comparing and aggregating $dM(t)/dt$, a common solution was implemented to derive $dM(t)/dt$ values from datasets of $\Delta M(t)$ only. Each $\Delta M(t)$ time series was used to generate a time-varying estimate of $dM(t)/dt$, $d[\Delta M(t)]/dt = dM(t)/dt$, and an estimate of the associated uncertainty, using a consistent approach. Time-varying estimates of $dM(t)/dt$ were computed by applying a sliding fixed-period window to the $\Delta M(t)$ time series. At each node, defined by the sampling period of the input time series, $dM(t)/dt$ and its standard error $\sigma_{dM(t)/dt}$ were estimated by fitting a linear trend to data within the window using a weighted least-squares approach, with each point weighted by its respective error variance $\sigma_{\Delta M(t)}^2$. The regression error $\sigma_{dM(t)/dt}$ incorporates measurement errors and model structural error due to any variability that deviates from linear trends in ice mass, and may be a conservative estimate in locations where such deviation is present. Time series of $dM(t)/dt$ computed using this approach were truncated by half the moving-average window period. When integrated, the $dM(t)/dt$ time series correspond to a low-pass-filtered version of the original $\Delta M(t)$ time series. This linear regression assumes that uncertainties are uncorrelated; however, the smoothing that we apply during the calculation of the trend causes data points to be correlated during several epochs beyond the sliding window.

Surface mass balance. Ice-sheet SMB comprises various processes governed by the interaction of the superficial snow and firn layers with the atmosphere. A direct mass exchange occurs via precipitation and surface sublimation. Snow drift and the formation of meltwater and its subsequent refreezing or retention redistribute mass spatially or lead to further mass loss via erosion and sublimation or via runoff. Here we compare a range of SMB products. Four SMB model solutions were considered for Antarctica (Extended Data Table 1): two regional models (RACMO2.3⁴⁰ and MARv3.6⁵²) and two global reanalysis products (JRA55⁵³ and ERA-Interim⁵⁴). The two regional climate models agree well in terms of their spatially integrated SMB, apart from the Peninsula where there is an offset of about 10 Gt per month between them (Extended Data Fig. 3). However, the reanalysis products underestimate the average SMB compared to the regional climate models by 200–350 Gt yr⁻¹. Our SMB assessment illustrates that products of similar class (climate models or reanalysis products) agree well, suggesting that groupings of their output may be appropriate. However, we found that model resolution is important when

estimating SMB and its components, because contributions that differed by only the spatial resolution yielded differences at the regional scale.

Glacial isostatic adjustment. GIA is the delayed response of the solid Earth to changes in time-variable surface loading through the growth and decay of ice sheets, and associated changes in sea level. Because GIA contributes to changes in the ice-sheet surface elevation and gravity field, it must be accounted for in measurements of the change in elevation and gravity for the purpose of isolating the contribution solely caused by ice-sheet imbalance. Here we compare different solutions derived from continuum-mechanical forward modelling to inform the interpretation of the satellite altimetry and gravimetry data that depend on the correction and to advise future assessments. Twelve GIA contributions were received that cover Antarctica (Extended Data Table 2), ten of which are global models^{22–29,31} and two of which are regional models³². Because a broad array of data may be used to constrain GIA forward models, we anticipate spread in the predictions.

Here we assess the degree of similarity between the various GIA model solutions. We identified areas of enhanced present-day vertical surface motion and (dis-)agreement between contributions by averaging the uplift rates over the contributions and computing the respective standard deviations (Extended Data Fig. 4). In some cases, it was necessary to estimate the GIA contribution to gravimetric mass trends; this was done using common geographical masks and truncation and a standardized treatment of low-degree harmonics. In Antarctica, the Amundsen Sea sector and the regions covered by the Ross and Filchner Ronne ice shelves stand out as having both high uplift rates (5–7 mm yr⁻¹ on average) and high variability in uplift rates (peaking at more than 10 mm yr⁻¹ standard deviation in the Amundsen sector) among the models considered. Elsewhere in coastal regions, uplift occurs at more moderate rates (about 2 mm yr⁻¹ on average); the interior of East Antarctica exhibits slow subsidence. In these regions, the average signal is accompanied by relatively low variance among the GIA models (0–1.5 mm yr⁻¹ standard deviation). None of the models fully captures portions of the uplift that are observed to be very large (see, for example, ref. ⁵⁵); hence, we anticipate a bias towards low values for the GIA correction averaged over such regions. In areas of low mantle viscosity, however, such as part of the WAIS, the GIA signal related to the Last Glacial Maximum may be overpredicted, and it is not clear whether a bias exists at the continental scale.

Differences between the model predictions arise for various additional reasons. Technical differences in the modelling approach, for example, relating to the consideration of self-gravitation, ocean loading, rotational feedback and compressibility, are most important at the global scale, but may explain only small differences among the regional models. Differing treatment of ice and ocean loading in regions that have experienced marine-based grounding-line retreat during the last glacial cycle may explain the differences in model predictions for the ICE_6G_C/VM5a combination (see Supplementary Table 1). Some small differences should be expected when comparing models that use spherical-harmonic and finite-element approaches. Looking beyond consideration of the model physics, larger differences arise owing to the various approaches used to determine the two principal unknowns associated with forward modelling of GIA—ice history and Earth rheology. There is no generally accepted ‘best approach’ to determining these inputs, and useful advances can be made by comparing the results of complementary approaches. In the models considered here, approaches to determining the ice history include dynamical ice-sheet modelling, coupled ice-sheet–GIA modelling, tuning to fit geodetic constraints, tuning to fit geological constraints and use of direct observations of historical ice-sheet change. When defining the rheological properties of the solid Earth, most studies have opted to use a Maxwell rheology to define a radially symmetric Earth; however, the use of a power-law rheology or a fully three-dimensional Earth model to capture the spatial complexity of mantle properties is increasingly popular. An intermediate approach used in many of the datasets included here has been to develop a regional GIA model that reflects local Earth structure. Such models can be tuned, albeit imperfectly, to provide as accurate a representation of GIA in that region as is possible. However, it remains a difficult and important challenge to incorporate these regional studies into a global framework. Finally, although four of the GIA models that we consider provide a measure of uncertainty, and several studies have used an ensemble modelling approach^{23,29}, an important future goal for the GIA modelling community is the inclusion of robust error estimates for all model predictions.

To compare the GIA models, we used Stokes coefficients that relate to their gravitational signal to determine the approximate magnitude of the effect of applying each correction to GRACE data (Extended Data Table 2). This is a preliminary assessment, because the effect of applying a GIA correction depends also on the methods used to process the GRACE data. Moreover, an agreement on the modelling of feedbacks has so far not been reached within the GIA community, leading to a large spread in the modelled degree-2 coefficients and possibly a strong bias when a correction is applied that is inconsistent with the GRACE observations (up to about 40 Gt yr⁻¹). In addition, none of the current GIA datasets includes estimates

of the GIA-induced geocentre motion (degree-1 coefficients). Therefore, we omit degree-1 and -2 coefficients in our assessment of the GIA-induced apparent mass change. From models that represent GIA in Antarctic only, we estimate that this omission could change the apparent mass-change value by up to 20%; however, this potential error is not currently included in the GIA error budget. There is relatively good agreement between the ten models that cover all of Antarctica (Extended Data Table 2); the estimated GIA contribution ranges from $+12 \text{ Gt yr}^{-1}$ to $+81 \text{ Gt yr}^{-1}$; the mean value is 56 Gt yr^{-1} . Although the solution from ref. ⁴⁴ is a notable outlier, it is the only one to account for three-dimensional variations in Earth's rheology. It will be interesting to compare this result with other such models that are under development.

Two of the GIA models^{32,56} are regional: although they cannot be compared with the continental-scale models directly, the magnitude of their signals is nonetheless included for interest.

Mass-balance intra-comparison. First, we compare estimates of mass change within each of the three geodetic-technique experiment groups to assess the degree to which results from common techniques concur and to derive individual, aggregated estimates of mass change from each technique. In each case, we compare estimated rates of mass change derived from a common technique over a common geographical region and over the full period of the respective datasets. Where datasets were computed using both drainage-basin definitions, we present the arithmetic mean of the two estimates. This is justified because the choice of drainage-basin set has a very small (less than 10 Gt yr^{-1}) effect on estimates of mass balance at the ice-sheet scale and even less at the regional scale. Within each experiment group, we perform an unweighted average of all individual data to obtain a single estimate of the rate of mass change per ice sheet for each geodetic technique. In a few cases, it was not possible to determine time-varying rates of mass change from individual estimates, because only constant rates of mass change and constant cumulative mass changes were supplied. Although the effect of averaging these datasets with time-varying solutions is to dampen the temporal variability present within the series of finer resolution, they are retained for completeness. We estimate the uncertainty of the average mass trends that emerge from each experiment group as the average of the errors associated with each individual estimate at each epoch.

To aid comparison, we (i) compute time-variable rates of mass change and their associated uncertainty over successive 36-month periods stepped in one-month intervals from time-varying cumulative mass changes, and (ii) average rates of mass change over one-year periods to remove signals associated with seasonal cycles. Time-varying rates of mass change are truncated at the start and end of each series to reflect the half-width of the time interval over which rates are computed, although this period is recovered on integration to cumulative mass changes. The extent to which we are able to analyse differences in mass-balance solutions that emerge from common satellite approaches is limited by the mismatch in temporal resolution of the individual datasets, which makes methodological and sampling differences difficult to separate.

Gravimetry mass-balance intra-comparison. Within the gravimetry experiment group, we assessed 15 estimates of mass balance derived from the GRACE satellites, in entirety spanning the period July 2002 to September 2016. Of these datasets, four^{57–60} were derived with direct imposition of the GRACE level-1 K-band range data. These impositions result in four different, independently derived, mascon approaches. Other methods often refer to 'mascon analysis', but are conducted on post-spherical-harmonic expansions and without imposing the level-1 K-band range data. We distinguish the later methods, referring to them as 'post-spherical-harmonic mascons'. Eleven contributions are derived from monthly spherical-harmonic solutions of the global gravity field using different approaches^{55,56,61–66}, which can be loosely classified as (i) region-integration approaches^{55,65,66}, (ii) post-spherical-harmonic mascon approaches^{56,61–63}, (iii) forward-modelling approaches^{62,64}, which essentially involve modelling of mass change with iterative comparison to the GRACE-derived signal, and (iv) approaches that use Slepian functions⁶⁷. One final estimate⁶⁸ made use of satellite altimetry data; although this estimate was excluded from our gravity ensemble average because it is a hybrid solution, it is presented alongside the gravimetry-only results for comparison. No restrictions were imposed on the choice of GIA correction; among the GRACE solutions we consider six different models^{21,24,26,30,31,43}. However, we did assess a wider set of nine continent-wide forward models and two regional models to better understand uncertainties in the GIA signal.

In total, there were 15 estimates of mass balance for each of the APIS, WAIS and EAIS. All were time-varying, cumulative mass-change solutions—the primary GRACE observable—and we computed time-varying rates of mass change from these data. Combining all of the individual mass-balance estimates, the effective (average) temporal resolution of the aggregated solution is one year. Further details of the gravimetry datasets and methods are included in Supplementary Table 1.

In Extended Data Fig. 5 we show a comparison of the rates of mass change obtained from all gravimetry mass-balance solutions, calculated over the three

main ice-sheet regions. At individual epochs, differences between time-varying rates of mass change are generally less than 50 Gt yr^{-1} in each ice-sheet region, and typically in the range $10\text{--}20 \text{ Gt yr}^{-1}$. Over the full period of the data, individual rates of mass balance for the APIS, WAIS and EAIS vary between -80 Gt yr^{-1} and $+10 \text{ Gt yr}^{-1}$, -260 Gt yr^{-1} and -20 Gt yr^{-1} , and -120 Gt yr^{-1} and $+200 \text{ Gt yr}^{-1}$, respectively. Considering all of the gravimetry data (Extended Data Table 3), the standard deviation of mass trends estimated during the period 2005–2015 is less than 24 Gt yr^{-1} in all three ice-sheet regions, with the largest spread occurring in the EAIS. In all three ice-sheet regions, the spread of individual mass balance estimates is well represented by the mean, considering the uncertainties of the individual and aggregated datasets.

Altimetry mass-balance intra-comparison. We assessed seven radar- and laser- altimetry-derived AIS mass-balance datasets, in entirety spanning the period April 1992 to July 2017. In total, six estimates of mass change were for the APIS, seven were for the EAIS and seven were for the WAIS. Of these, four included data from radar altimetry and six from laser altimetry. Various techniques were used to derive the elevation and mass trends^{69–75}. Only two of the altimetry datasets were time series of cumulative mass change, from which we computed time-varying rates of mass change. The remaining altimetry datasets were constant rates of mass change, which appear in our altimetry average as time-invariant solutions. The period over which altimetry rates of mass change were computed ranged from 2 years to 24 years. In consequence, the aggregated dataset has a temporal resolution that is lower than annual. Including all individual mass-balance datasets, the effective (average) temporal resolution of the aggregated solution is 3.3 years. Further details of the altimetry datasets and methods are included in Supplementary Table 1.

With a few exceptions, rates of mass change determined from radar and laser altimetry tend to differ by less than 100 Gt yr^{-1} at all times in each ice-sheet region (Extended Data Fig. 5). The main exceptions are in the EAIS, where one estimate⁷⁴ reports mass trends that are roughly 100 Gt yr^{-1} more positive than all others during the ERS and ICESat periods, and in the WAIS, where two estimates^{71,74} report rates that are about 70 Gt yr^{-1} less negative than the others during the ICESat period. Among the remaining datasets, the closest agreement occurs at the APIS, where mass trends agree to within 30 Gt yr^{-1} at all times; the poorest agreement occurs at the EAIS, where mass trends depart by up to 100 Gt yr^{-1} . The largest differences are between datasets that are constant in time during periods where rapid changes in mass balance occur in the annually resolved time series, suggesting that a proportion of the difference is due to their poor temporal resolution. Mass-balance solutions from the relatively short (six-year) ICESat mission also appear to show larger spreads compared to those determined from longer (decade-scale) radar- altimetry missions. This larger spread is due in part to differences in the bias-correction models applied to ICESat data^{74,76–78} and in part to the large influence of firn densification on altimetry measurements over short periods, which have been corrected for using different models. Firn-densification models are generally not applied to mass-balance solutions determined from radar altimetry. Further analysis of the corrections for bias between ICESat campaigns and firn compaction is required to establish the statistical significance of the differences and to reduce their collective uncertainty. Comparing rates of mass change (Extended Data Table 3), the average standard deviation of all mass trends at each epoch over the common period 2005–2015 is less than 54 Gt yr^{-1} in all four ice-sheet regions. The largest spread between the individual values occurs in the EAIS. Other than this sector, the individual estimates lie close to the ensemble average, considering the respective uncertainty of the measurements.

Input-output-method intra-comparison. Although the input–output method is the most direct measure of changes in mass fluxes, a key difficulty is that, to assess mass balance, it must differentiate between two large numbers—one for annual SMB and the other for discharge plus grounding-line migrations—and deal appropriately with the error budgets of both. A consequence of this complexity is that few input–output-method datasets exist at the ice-sheet scale. Here we collate just two input–output-method datasets, both based on the same method⁷⁹—far fewer than were considered for altimetry and gravimetry. The first dataset spans the period 1992–2010¹⁸; the second is limited to the period 2002–2016. The same SMB model (RACMO2.3) was used in both assessments. Further details of the input–output-method datasets and methods are included in Supplementary Table 1.

We compare the two datasets during the period 2002–2010 (when the datasets overlap; Extended Data Table 3). The smallest differences (up to 30 Gt yr^{-1}) arise in the APIS and the WAIS; the largest differences (up to 70 Gt yr^{-1}) occur at the EAIS. In all cases, the average difference between estimates of mass balance derived from each dataset is comparable to the estimated uncertainty. Including both datasets, rates of mass balance over the period 1992–2016 for the APIS, WAIS and EAIS range from -125 Gt yr^{-1} to $+25 \text{ Gt yr}^{-1}$, -300 Gt yr^{-1} to $+100 \text{ Gt yr}^{-1}$ and -200 Gt yr^{-1} to $+200 \text{ Gt yr}^{-1}$, respectively (Extended Data Fig. 5). The origin of the differences between the two datasets requires further investigation.

Ice-sheet mass-balance inter-comparison. To assess the degree to which the satellite techniques concur, we used the aggregated time series from each

geodetic-technique experiment group to compute changes in ice-sheet mass balance within common geographical regions and over a common interval of time (the overlap period). We calculate the aggregated time series as the arithmetic mean of all available rates of ice-sheet mass balance derived from the same satellite technique at each available epoch. We used the individual ice sheets and their integrals as common geographical regions. The maximum duration of the overlap period is limited to the 14-year interval (2002–2016) when all three satellite techniques were optimally operational. However, we also considered the availability of mass-balance datasets, which leads us to select the period 2003–2010 as the optimal interval (see Fig. 1). When the aggregated mass-balance data from all three experiment groups are degraded to a common temporal resolution of 36 months, the time series are on average well correlated ($0.5 < r^2 < 0.9$) at the APIS and WAIS. At the EAIS, however, the aggregated altimetry mass-balance time series are poorly correlated ($r^2 < 0.1$) in time with the aggregated gravimetry and input–output-method data. Possible explanations for this include the relatively high short-term variability in mass fluctuations in this region, the relatively low trend in mass and the heterogeneous temporal resolution of the aggregated altimetry dataset. Over longer periods, marked increases in the rate of mass loss from the WAIS are also recorded in all three satellite datasets.

Because the comparison period is long in relation to the timescales over which SMB fluctuations typically occur, their potential effect on the overall inter-comparison is reduced. The closest agreement between individual estimates of ice-sheet mass balance occurs at the APIS and the WAIS, where the standard deviation across all techniques is 15–41 Gt yr⁻¹ (Extended Data Table 4). The greatest departure occurs at the EAIS, where the input–output-method and gravimetry estimates of mass balance differ by about 80 Gt yr⁻¹ and the standard deviation of all three estimates is about 40 Gt yr⁻¹. This high degree of variance is expected because of the relatively large size of the region, the small amplitude of signals and the poor independent controls on coastal SMB. When compared to the inter-technique mean and standard deviation, all estimates of ice-sheet mass balance determined from the individual satellite techniques are now in agreement, given their respective uncertainties. In contrast to the first IMBIE assessment¹⁸, this finding also now holds at continental and global scales. We therefore conclude that estimates of mass balance determined from independent geodetic techniques agree when compared to their respective uncertainties.

Several noteworthy patterns in the distribution of mass-balance estimates determined during the overlap period (2003–2010) merit further discussion. Estimates of mass balance derived from satellite altimetry and gravimetry agree to within 15 Gt yr⁻¹ on average and with the mean of all three techniques, in all ice-sheet regions. By contrast, estimates of mass balance determined from the input–output method are 55 Gt yr⁻¹ more negative on average than the mean in all ice-sheet regions. However, despite the bias, the input–output-method estimates remain in agreement because their estimated uncertainties are relatively large (approximately three times larger than those of the other techniques). A more detailed analysis of the primary and ancillary datasets is required to establish whether this bias is significant or systematic.

Ice-sheet mass-balance integration. We combined estimates of ice-sheet mass balance derived from each geodetic-technique experiment group to produce a single, reconciled estimate, following the same approach as for the first assessment. This estimate was computed as the arithmetic mean of the average rates of mass change from each experiment group, within the regions of interest and at the time periods for which the experiment-group mass trends were determined. We estimated the uncertainty of the mass-balance data using the following approach. Within each experiment group, we estimated the uncertainty of mass trends as the average of the errors associated with each individual estimate and the uncertainty of reconciled rates of mass change (see, for example, Table 1) as the root-mean-square of the uncertainties associated with mass trends from each experiment group. When summing mass trends of multiple ice sheets, the combined uncertainty was estimated as the root-sum-square of the uncertainties for each region. Finally, to estimate the cumulative uncertainty of mass changes over time, we weighted the annual uncertainty by $1/\sqrt{n}$, where n is the number of years since the start of each time series, and summed the weighted annual uncertainties over time⁸⁰.

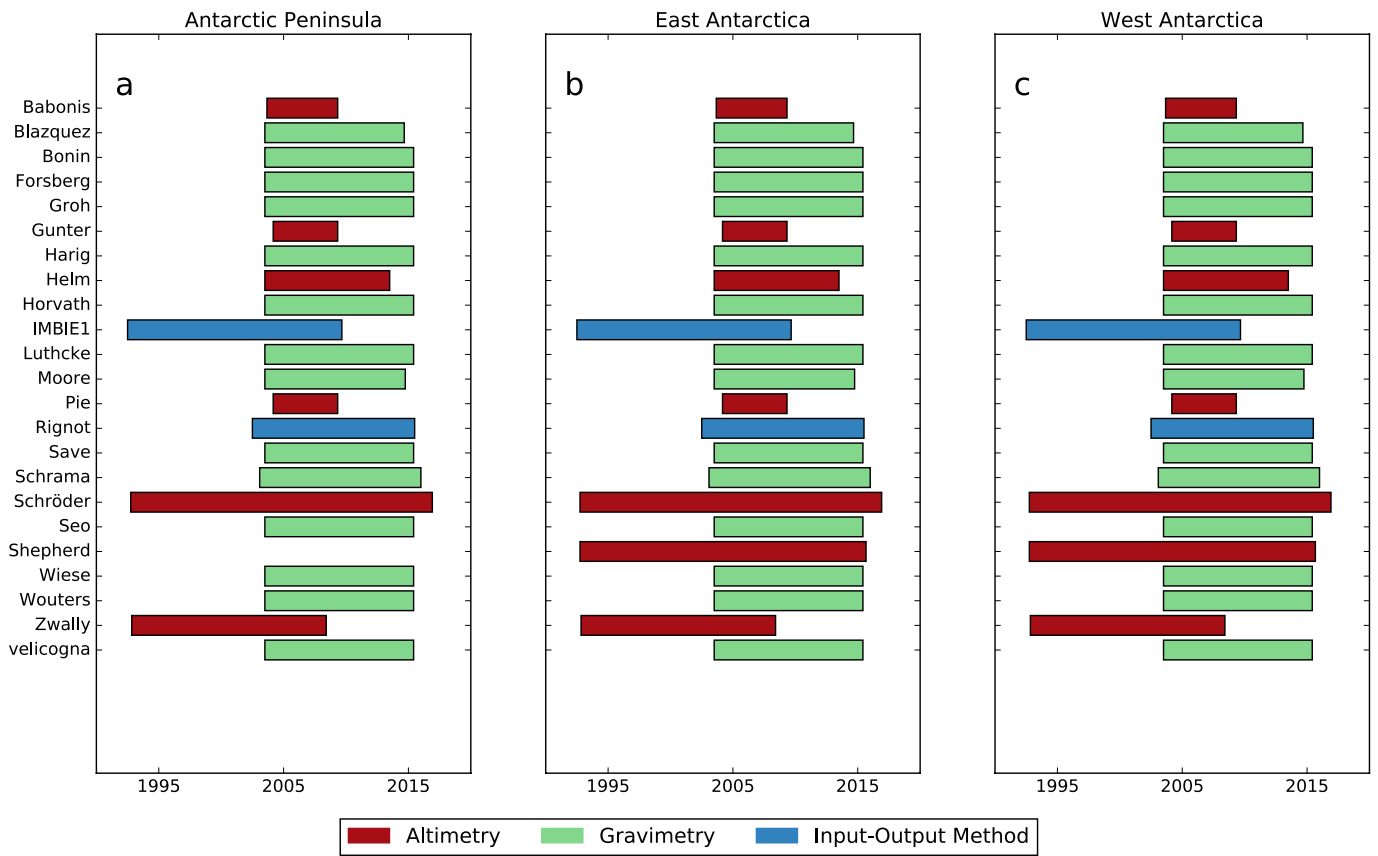
Across the full 25-year survey, the average rate of mass balance of the AIS was -109 ± 56 Gt yr⁻¹ (Table 1). To investigate inter-annual variability, we also calculated mass trends during successive five-year intervals. Whereas the APIS and WAIS each lost mass throughout the entire survey period, the EAIS experienced alternating periods of mass loss and mass gain, probably driven by inter-annual fluctuations in SMB. The rate of mass loss from the WAIS has increased over time owing to accelerated ice discharge in the Amundsen Sea sector^{33,47,73,81–83}. The largest increase—a doubling of the rate of ice loss—occurred between the periods 2002–2007 and 2007–2012 (Table 1). Overall, the WAIS accounts for the vast majority of ice-mass losses from Antarctica. At the APIS, rates of ice-mass loss since the early 2000s are notably higher than during the previous decade,

consistent with observations of surface lowering^{71,73} and increased ice flow in southerly glacier catchments⁸⁴. The approximate state of balance of the wider EAIS suggests that the reported dynamic thinning of the Totten and Cook glaciers^{85,86} has been offset by accumulation gains elsewhere⁸⁷.

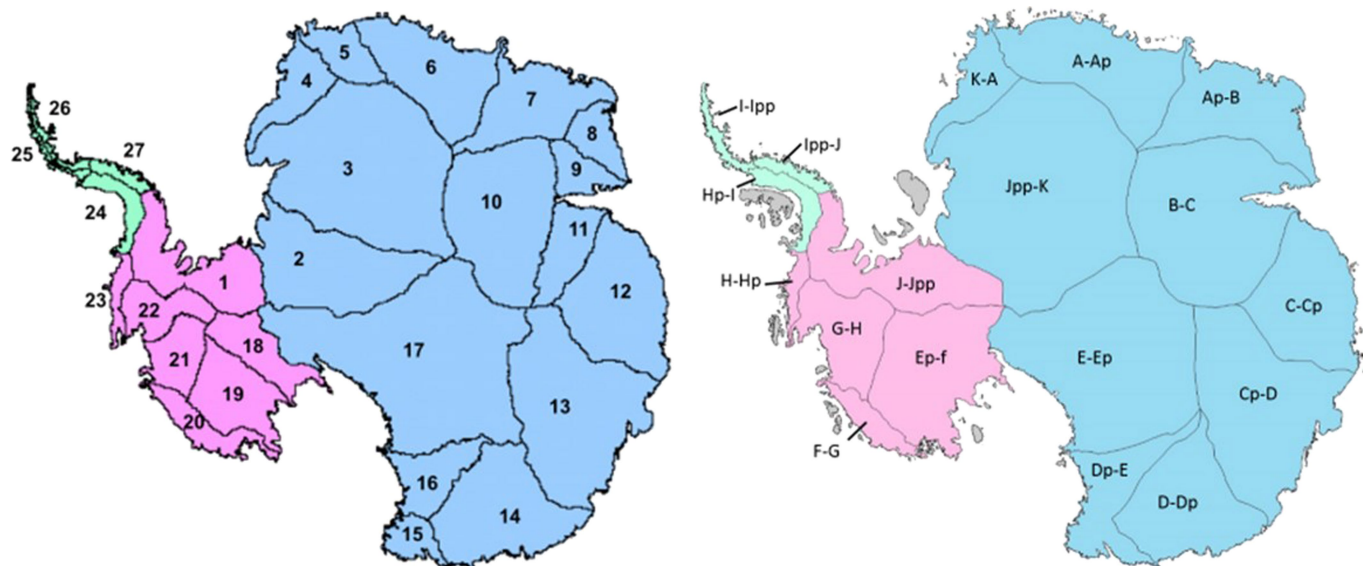
Data availability. The final mass-balance datasets generated in this study are freely available at <http://www.imbie.org/data-downloads>.

52. Fettweis, X. et al. Estimating the Greenland ice sheet surface mass balance contribution to future sea level rise using the regional atmospheric climate model MAR. *Cryosphere* **7**, 469–489 (2013).
53. Kobayashi, S. et al. The JRA-55 reanalysis: general specifications and basic characteristics. *J. Meteorol. Soc. Jpn.* **93**, 5–48 (2015).
54. Dee, D. P. et al. The ERA-Interim reanalysis: configuration and performance of the data assimilation system. *Q. J. R. Meteorol. Soc.* **137**, 553–597 (2011).
55. Groh, A. & Horwath, M. The method of tailored sensitivity kernels for GRACE mass change estimates. *Geophys. Res. Abstr.* **18**, 12065 (2016).
56. Barletta, V. R., Sørensen, L. S. & Forsberg, R. Scatter of mass changes estimates at basin scale for Greenland and Antarctica. *Cryosphere* **7**, 1411–1432 (2013).
57. Luthcke, S. B. et al. Antarctica, Greenland and Gulf of Alaska land-ice evolution from an iterated GRACE global mascon solution. *J. Glaciol.* **59**, 613–631 (2013).
58. Andrews, S. B., Moore, P. & King, M. A. Mass change from GRACE: a simulated comparison of Level-1B analysis techniques. *Geophys. J. Int.* **200**, 503–518 (2015).
59. Save, H., Bettadpur, S. & Tapley, B. D. High-resolution CSR GRACE RLO5 mascons. *J. Geophys. Res. Solid Earth* **121**, 7547–7569 (2016).
60. Watkins, M. M., Wiese, D. N., Yuan, D. N., Boeninger, C. & Landerer, F. W. Improved methods for observing Earth's time variable mass distribution with GRACE using spherical cap mascons. *J. Geophys. Res. Solid Earth* **120**, 2648–2671 (2015).
61. Schrama, E. J. O., Wouters, B. & Rietbroek, R. A mascon approach to assess ice sheet and glacier mass balances and their uncertainties from GRACE data. *J. Geophys. Res. Solid Earth* **119**, 6048–6066 (2014).
62. Seo, K. W. et al. Surface mass balance contributions to acceleration of Antarctic ice mass loss during 2003–2013. *J. Geophys. Res. Solid Earth* **120**, 3617–3627 (2015).
63. Velicogna, I., Sutterley, T. C. & van den Broeke, M. R. Regional acceleration in ice mass loss from Greenland and Antarctica using GRACE time-variable gravity data. *Geophys. Res. Lett.* **41**, 8130–8137 (2014).
64. Wouters, B., Bamber, J. L., van den Broeke, M. R., Lenaerts, J. T. M. & Sasgen, I. Limits in detecting acceleration of ice sheet mass loss due to climate variability. *Nat. Geosci.* **6**, 613–616 (2013).
65. Blazquez, A. et al. Exploring the uncertainty in GRACE estimates of the mass redistributions at the Earth surface. *Implications for the global water and sea level budgets*. (submitted).
66. Horwath, A. G. *Retrieving Geophysical Signals from Current and Future Satellite Missions*. PhD thesis, Tech. Univ. Munich (2017).
67. Harig, C. & Simons, F. J. Mapping Greenland's mass loss in space and time. *Proc. Natl Acad. Sci. USA* **109**, 19934–19937 (2012).
68. Rietbroek, R., Brunnabend, S. E., Kusche, J. & Schröder, J. Resolving sea level contributions by identifying fingerprints in time-variable gravity and altimetry. *J. Geodyn.* **59–60**, 72–81 (2012).
69. Babonis, G. S., Csatho, B. & Schenk, T. Mass balance changes and ice dynamics of Greenland and Antarctic ice sheets from laser altimetry. In *International Archives of the Photogrammetry, Remote Sensing and Spatial Information Sciences* Vol. XLI-B8 (eds Zdimas, V. et al.) 481–487 (ISPRS, 2016).
70. Felikson, D. et al. Comparison of elevation change detection methods from ICESat altimetry over the Greenland Ice Sheet. *IEEE Trans. Geosci. Remote Sens.* **55**, 5494–5505 (2017).
71. Helm, V., Humbert, A. & Miller, H. Elevation and elevation change of Greenland and Antarctica derived from CryoSat-2. *Cryosphere* **8**, 1539–1559 (2014).
72. Ewert, H. et al. Precise analysis of ICESat altimetry data and assessment of the hydrostatic equilibrium for subglacial Lake Vostok, East Antarctica. *Geophys. J. Int.* **191**, 557–568 (2012).
73. McMillan, M. et al. Increased ice losses from Antarctica detected by CryoSat-2. *Geophys. Res. Lett.* **41**, 3899–3905 (2014).
74. Zwally, H. J. et al. Mass gains of the Antarctic ice sheet exceed losses. *J. Glaciol.* **61**, 1019–1036 (2015).
75. Gunter, B. C. et al. Empirical estimation of present-day Antarctic glacial isostatic adjustment and ice mass change. *Cryosphere* **8**, 743–760 (2014).
76. Scambos, T. & Shuman, C. Comment on 'Mass gains of the Antarctic ice sheet exceed losses' by H. J. Zwally and others. *J. Glaciol.* **62**, 599–603 (2016).
77. Zwally, H. J. et al. Response to Comment by T. SCAMBOS and C. SHUMAN (2016) on 'Mass gains of the Antarctic ice sheet exceed losses' by H. J. Zwally and others (2015). *J. Glaciol.* **62**, 990–992 (2016).
78. Richter, A. et al. Height changes over subglacial Lake Vostok, East Antarctica: insights from GNSS observations. *J. Geophys. Res. Earth Surf.* **119**, 2460–2480 (2014).
79. Rignot, E., Velicogna, I., van den Broeke, M. R., Monaghan, A. & Lenaerts, J. Acceleration of the contribution of the Greenland and Antarctic ice sheets to sea level rise. *Geophys. Res. Lett.* **38**, L05503 (2011).
80. Stocker, T. F. et al. (eds) *Climate Change 2013: the Physical Science Basis. Working Group I Contribution to the Fifth Assessment Report of the Intergovernmental Panel on Climate Change* Ch. 4 (Cambridge Univ. Press, New York, 2013).
81. Bouman, J. et al. Antarctic outlet glacier mass change resolved at basin scale from satellite gravity gradiometry. *Geophys. Res. Lett.* **41**, 5919–5926 (2014).

82. Konrad, H. et al. Uneven onset and pace of ice-dynamical imbalance in the Amundsen Sea embayment, West Antarctica. *Geophys. Res. Lett.* **44**, 910–918 (2017).
83. Gardner, A. S. et al. Increased West Antarctic and unchanged East Antarctic ice discharge over the last 7 years. *Cryosphere* **12**, 521–547 (2018).
84. Hogg, A. E. et al. Increased ice flow in Western Palmer Land linked to ocean melting. *Geophys. Res. Lett.* **44**, 4159–4167 (2017).
85. Pritchard, H. D., Arthern, R. J., Vaughan, D. G. & Edwards, L. A. Extensive dynamic thinning on the margins of the Greenland and Antarctic ice sheets. *Nature* **461**, 971–975 (2009).
86. Li, X., Rignot, E., Morlighem, M., Mouginot, J. & Scheuchl, B. Grounding line retreat of Totten Glacier, East Antarctica, 1996 to 2013. *Geophys. Res. Lett.* **42**, 8049–8056 (2015).
87. Lenaerts, J. T. M. et al. Recent snowfall anomalies in Dronning Maud Land, East Antarctica, in a historical and future climate perspective. *Geophys. Res. Lett.* **40**, 2684–2688 (2013).
88. Pollard, D. & Deconto, R. M. Description of a hybrid ice sheet-shelf model, and application to Antarctica. *Geosci. Model Dev.* **5**, 1273–1295 (2012).
89. Martinec, Z. Spectral-finite element approach to three-dimensional viscoelastic relaxation in a spherical earth. *Geophys. J. Int.* **142**, 117–141 (2000).

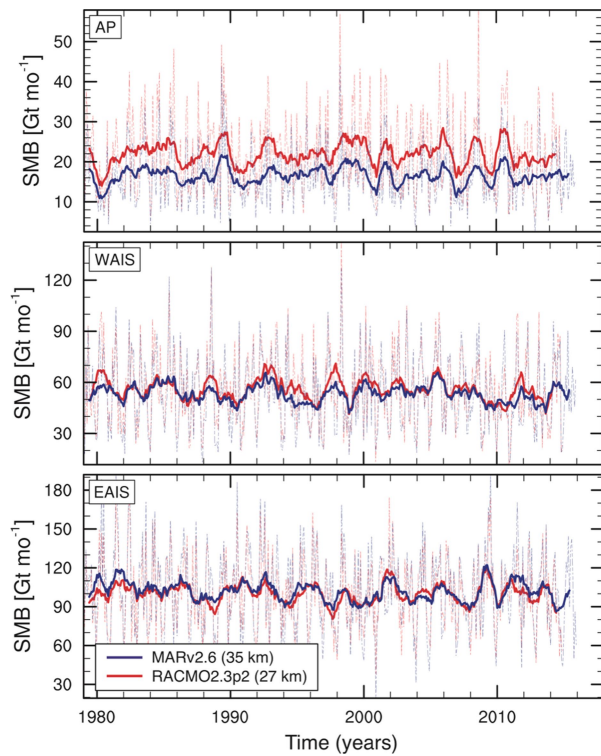


Extended Data Fig. 1 | Datasets of ice-sheet mass balance included in our assessment. Details about the datasets are provided in Supplementary Table 1. Some datasets did not encompass all three ice sheets.

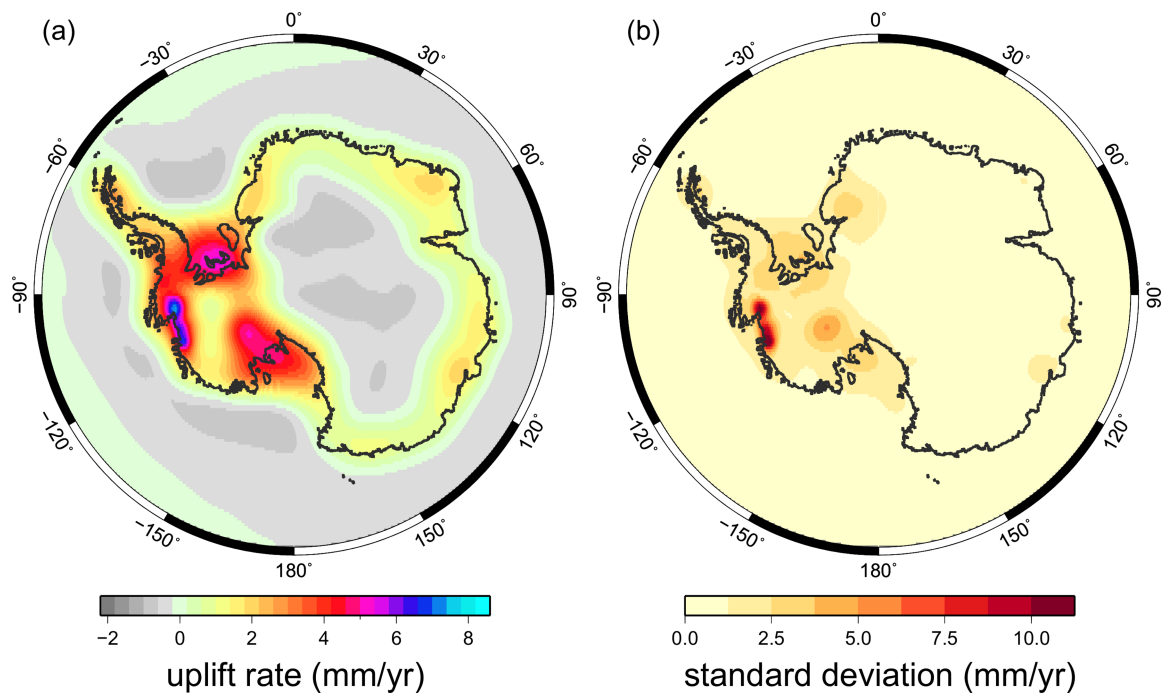


Extended Data Fig. 2 | Ice-sheet drainage basins. AIS drainage basins are determined according to the definitions of ref. ³ (left) and refs ^{2,19} (right). Basins that fall within the Antarctic Peninsula, West Antarctica and East Antarctica are shown in green, pink and blue, respectively. For the definition from ref. ³, the Antarctic Peninsula, West Antarctica and

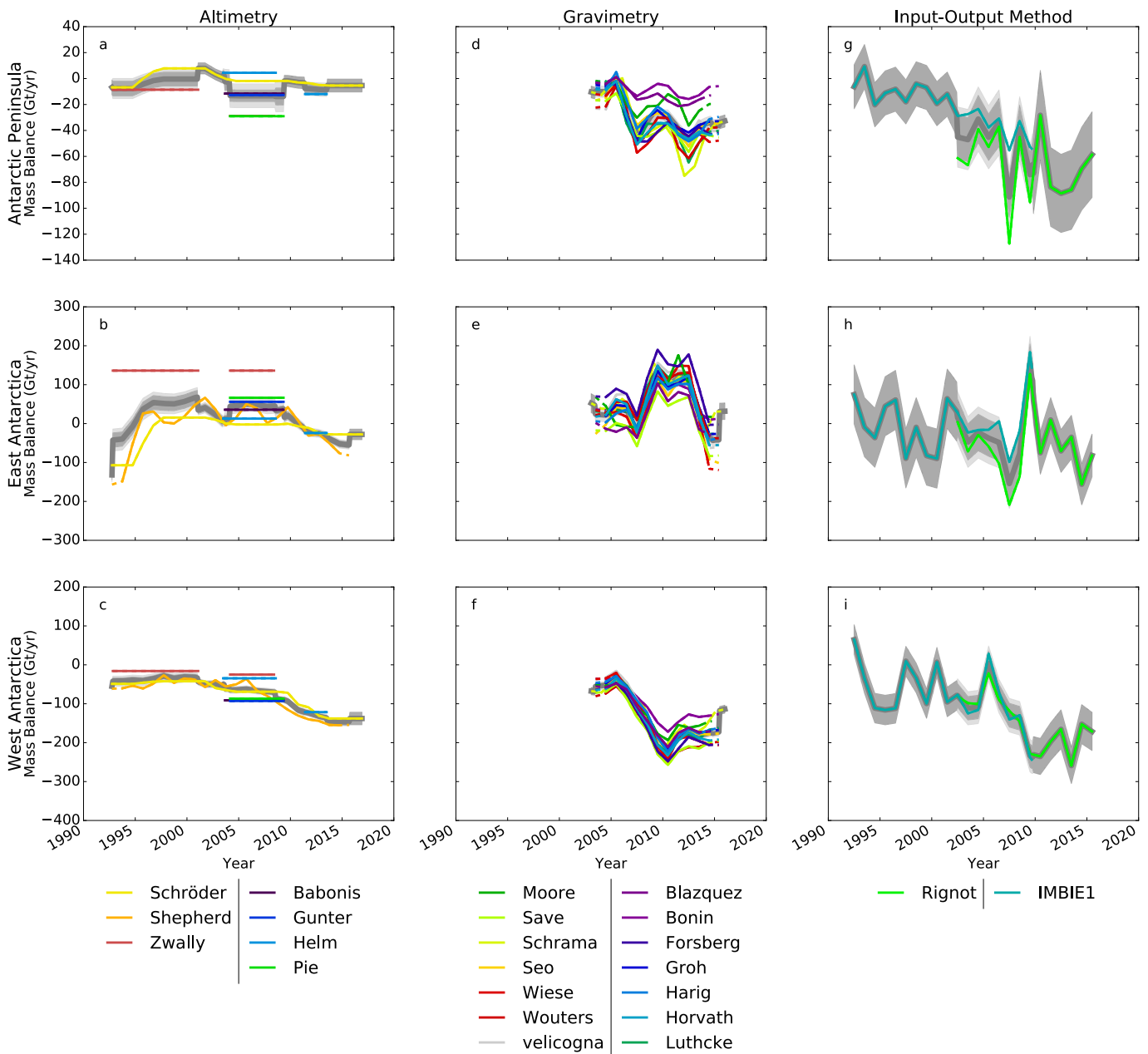
East Antarctica basins cover areas of 227,725 km², 1,748,200 km² and 9,909,800 km², respectively. For the definition from refs ^{2,19}, the Antarctic Peninsula, West Antarctica and East Antarctica basins cover areas of 232,950 km², 2,039,525 km² and 9,620,225 km², respectively.



Extended Data Fig. 3 | Temporal variations in AIS SMB. We show time series of integrated SMB in AIS drainage regions^{2,19} from the MARv2.6 (blue) and RACMO2.3p2 (red) models. Solid lines are annual averages of the monthly data (dashed lines). mo, month.



Extended Data Fig. 4 | Modelled GIA beneath the AIS. **a**, Bedrock uplift rates in Antarctica averaged over the GIA model solutions used in this assessment. **b**, The corresponding standard deviations.



Extended Data Fig. 5 | Individual rates of ice-sheet mass balance. a–i, Mass-balance estimates were determined from satellite altimetry (a–c), gravimetry (d–e) and the input–output method (g–i) for the Antarctic Peninsula (a, d, g), East Antarctica (b, e, h) and West

Antarctica (c, f, i). The light-grey shading shows the estimated 1σ uncertainty relative to the ensemble average. The standard error of the mean solutions, per epoch, is shown in mid-grey.

Extended Data Table 1 | Spatially averaged AIS SMB

Model	Class	Area (10 ⁶ km ²)	Grid	SMB (Gt/yr)
RACMO2.3	RCM	12.30	27km	2004
RACMO2.3p2	RCM	12.30	27km	2107
MARv3.6.40	RCM	12.32	35km	2150
ERA-Interim	GCM	12.20	80km	1900
JRA55	GCM	12.24	55km	1807

Estimates of the average SMB over the period 1980–2012 were derived from regional climate models (RCM) and global reanalyses (GCM). Data were evaluated using the drainage basins from refs ^{2,19}.

Extended Data Table 2 | GIA model details

Model	Publication ^a	Ice sheet	Earth model ^b	Ice model ^c	GIA model ^d	Constraint data ^e	Mass change (Gt/yr)
A13	⁸	AIS	VM5a (1D) ⁱ	ICE-6G_C	SH, C, RF, SG, OL	As for ICE-6G_C	+68 [‡]
AGE1a	⁹	AIS	ensemble of regional 1D models	Own model: ice thickness scaled to fit GPS	SH(256), UQ	GPS	+48 ± 14 [‡]
DIEM/ANT1D.0	¹⁰	AIS	1D (90,0.5,20)	Dynamically coupled model ^j	SH(170) ^k ; dynamically coupled model	GPS, RSL	+49 [‡]
ICE-6G_C (VM5a)	⁵	AIS	VM5a (1D) ⁱ	ICE-6G_C	SH(1024)	GPS, RSL, Earth rotation	+72 [‡]
ICE-6G_D (VM5a)	⁵	AIS	VM5a (1D) ⁱ	ICE-6G_D ^f	SH(512)	GPS, RSL, Earth rotation	+62 [‡]
SL-dry-4mm/W12	¹¹	AIS	3D, power-law rheology	Combination of W12 and ICE-5G	FE, IC, xRF	GPS, RSL, seismic velocities (earth model)	+12 [‡]
W12a	¹²	AIS	1D (120,1,10)	Own model: dynamic, time slice	SH(256), C, RF, SG, OL, UQ	GPS, RSL, ice extent & thickness	+56 ± 27 [‡]
SELEN 4	¹³	AIS	VM5a (3-layer average of 1D model) ⁱ	ICE-6G_C	SELEN4: SH(128), IC, RF, SG, OL	As for ICE-6G_C	+81 [‡]
GLAC1-D	¹⁴	AIS	VM5a (1D) ⁱ	Own coupled model: dynamic, from ensemble	SH(512), IC, SG, OL, xRF	RSL, ice extent & thickness, present ice sheet	+55 [‡]
IJ05_R2	¹⁵	AIS	1D (65,0.2,4)	Own model	SH(256), IC, SG, OL, UQ	GPS, ice extent & thickness	+55 ± 13 [‡]
NAP_N14	¹⁶	nAPIS ^g	1D (130, 0.0007,0.4,10)	Own model: 1995-present	SH(1195), C, SG, xRF, xOL	GPS, altimetry & DEM difference (ice model)	+3 [‡]
ASE14G (L60S186)	¹⁶	AS ^h	1D (60, 0.00398,0.0158,0.025)	Own model: 1900-present	SH(1195), C, SG	GPS, altimetry (ice model)	+19 [‡]

[‡]Regional changes in mass associated with the GIA signal were determined from the model data.

[‡]Regional changes in mass associated with the GIA signal were calculated as an indicative rate using spherical-harmonic degrees 3 to 90.

^aMain publication^{5,8-16} listed; supporting publications are provided in Supplementary Table 1.

^bModel from main publication unless otherwise stated. Comma-separated values refer to properties of a radially varying (1D, one-dimensional) Earth model: the first value is lithosphere thickness (km); other values reflect mantle viscosity ($\times 10^{21}$ Pa s) for specific layers; see relevant publications for details.

^cIce model covers at least the Last Glacial Maximum to present, unless otherwise indicated.

^dGIA model details: SH, spherical harmonic (maximum degree indicated in parentheses); FE, finite element; C, compressible; IC, incompressible; RF, rotational feedback; SG, self-gravitation; OL, ocean loading; x, feature not included; UQ, uncertainty quantified.

^eRSL, relative sea-level data; GPS rates were all corrected for the elastic response to contemporary ice mass change.

^fDifferent to ICE-6G_C in Antarctica, owing to the use of BEDMAP2¹ topography in that region.

^gModel relates to GIA in the northern Antarctic Peninsula (nAPIS) only.

^hModel relates to GIA in the Amundsen Sea (AS) embayment only.

ⁱEarth model from ref. ²⁴.

^jIce model from ref. ⁸⁸.

^kGIA model from ref. ⁸⁹.

Extended Data Table 3 | Features of mass-balance datasets included in our assessment

Region	Technique	Span (years)	Temporal resolution (months)	dM/dt range (Gt/yr)	dM/dt error (Gt/yr)	dM/dt standard deviation (Gt/yr)
APIS	Gravimetry	2005 to 2015	1 to 12	-39 to -9	1 to 24	10
WAIS	Gravimetry	2005 to 2015	1 to 12	-177 to -114	1 to 30	16
EAIS	Gravimetry	2005 to 2015	1 to 12	+11 to +107	2 to 35	24
APIS	Altimetry	1992 to 2017	1 to 8.25	-29 to -3	2 to 17	12
WAIS	Altimetry	1992 to 2017	1 to 8.25	-97 to -25	4 to 39	27
EAIS	Altimetry	1992 to 2017	1 to 8.25	-11 to +136	10 to 52	54
APIS	Mass Budget	1992 to 2016	1	-120 to +20	30	35
WAIS	Mass Budget	1992 to 2016	1	-250 to +100	2	61
EAIS	Mass Budget	1992 to 2016	1	-200 to +200	65	95

Details shown include the maximum span, temporal sampling, amplitude, estimated error and standard deviation at each epoch.

Extended Data Table 4 | Aggregated estimates of ice-sheet mass balance from satellite altimetry, gravimetry and the input–output method

Region	Altimetry mass balance (Gt/yr)	Gravimetry mass balance (Gt/yr)	Mass budget mass balance (Gt/yr)	Average mass balance (Gt/yr)
EAIS	37 ± 18	47 ± 18	-35 ± 65	15 ± 41
WAIS	-70 ± 8	-101 ± 9	-115 ± 43	-93 ± 26
APIS	-10 ± 9	-23 ± 5	-51 ± 24	-27 ± 15
AIS	-43 ± 21	-76 ± 20	-201 ± 82	-105 ± 51

In this comparison, the data were averaged over the period 2003–2010. The arithmetic mean of each individual result is also shown for the given regions, along with the combined imbalance of the AIS, calculated as the sum of estimates from the constituent regions.